A nanosecond pulsed discharge circuit model for engine applications

Vyaas Gururajan, Riccardo Scarcelli

Argonne National Laboratory, 9700 S. Cass. Ave, Lemont, IL 60439, USA

E-mail: `vgururajan@anl.gov`

June 2021

Abstract.

Non-equilibrium plasma discharges in spark gaps have been an increasingly studied method for alleviating cycle to cycle variation in lean and dilute combustion environments. However, ignition models that account for streamer propagation, cathode fall, and transmission line amplification over nanosecond time scales have so far not been developed. The present study develops such a model, with emphasis on the energy delivered from *circuit to cylinder*. Key pieces of the relevant physics and chemistry are summarized, simplified, and systematically coupled to one another. The set of parameters is limited to a handful of key observables and modeled using Modelica. Results show non-trivial behavior in the energy delivery characteristics of such discharges with important implications for ignition.

1. Introduction

The ignition of flames in Spark Ignition Engines is triggered by a high temperature plasma discharge. The temperature is high enough to counter the effects of heat and radical loss (which would otherwise quench the flame), and thus promote the expansion of the incipient flame kernel. Such a triggering event is possible using *low temperature plasma* (LTP) discharges as well. The advantages of using LTP discharges for SI engines are:

(i) Volumetric flexibility: LTP discharges can occupy larger volumes than HTP discharges [1].

(ii) Temporal flexibility: Nanosecond pulsed discharges can be issued repeatedly without depositing large currents, thus enhancing the prospect of lean ignition and overcoming the ignition related origins of cycle to cycle variation (CCV) [2].

(iii) Lower electrode erosion: Smaller currents imply smaller ion fluxes and therefore lower electrode erosion [3].

A current trend in improving the fuel economy of vehicles is to increase the compression ratio while using Exhaust Gas Recirculation (EGR) to control knock and reduce NOx [4]. But at higher rates of EGR, CCV begins to dominate, partly because flame initiation becomes more challenging [5]. Nanosecond pulsed LTP discharges can address this problem.

While experiments showing the promise of repeated LTP discharges in engines to suppress CCV have been carried out [2], first principles based simulation efforts have been restricted to simpler configurations where the geometry of the electrodes is canonical, and the range of pressures and mixture compositions is limited [6][7]. The paucity of data interrelating the important parameters of LTP discharges makes the verification and validation of discharge simulations, of any dimensionality, that much more challenging.

Conventional spark modeling for the purpose of ignition simulations is a more mature enterprise. The advantage in modeling a thermal spark subject to long time scale velocity perturbations [8] is that the convective heat transfer characteristics can be used to establish a relationship between current and voltage [9]. This has been exploited in ignition models that take into account the effect of the circuit [10]. However, such heat transfer relations are inapplicable to nanosecond pulsed discharges owing to the drastically different timescales involved. Nanosecond pulsed discharges last over timescales that are comparable to the transmission timescales of voltage pulses from the source to the electrodes. This can lead to reflection of energy from the electrodes [11], and needs to be accounted for in both measurement and simulation if an accurate estimate of the incipient flame kernel is desired.

Self-similarity models that take into account the role of shock wave losses [12] are also inapplicable due to the non-equilibrium nature of electron energy distribution.

First principle streamer (a.k.a. ionization wave) simulations have progressed over the last decade, significantly clarifying the underlying processes, but problems persist:

(i) The timescale over which the electric field in a plasma changes is inversely proportional to the electron number density, as electrons are the most mobile species and consequently tend to *screen* out the applied field the fastest [13] . Although streamers propagate over a fraction of a nanosecond and can be adequately resolved by second-order accurate methods with time-step sizes of $\sim 10^{-12}$ s, resolving the electron evolution in the bridged gap requires much smaller time-steps, often as small as $\sim 10^{-14}$ s for just 1 atm simulations. Fixes for this problem have been proposed [14], but are found to introduce artefacts that can significantly interfere with the evolution of the plasma. At higher pressures, the spatial resolution required to resolve the bridged gap significantly increases.

(ii) Streamer simulations are often limited by the assumptions in their premises. For instance, the Local Field Approximation (LFA), as simple as it is to formulate, is known to have its shortcomings [15]. Streamer branching is better captured in discrete particle simulations compared to their continuum counterpart [16]. And it is not fully clear if multiple temperature models are entirely sufficient for the simulation of ignition [17].

Given these problems, it is worthwhile to develop reduced order models, akin to the aforementioned spark models, so that investigation into CCV is not stalled by inabilities to capture details that are subject to large uncertainties. Recent work has shown the utility in developing such models to describe flame ignition due to multiple LTP discharges [18]. It was found that the key quantities that determine ignitability are the energy deposited and the volume of the discharge.

The main goal of the present study is to furnish a simple model that accounts for the energy deposited in a high pressure LTP discharge given a small number of parameters related to key observables of the discharge and circuit, much like what has been done previously at low pressures by Adamovich et al [19]. The model is intended to be straightforwardly coupled with engine simulations, completely accounting for the energy conveyed from circuit to cylinder. Such a model enables a numerical inquiry into the role of nanosecond pulsed LTP discharges in reducing CCV.

2. Modeling the LTP discharge

The phenomenon of an LTP discharge in a conventional spark gap ($\approx$ 0.5 mm) can be summarized as follows (see Raizer's textbooks for details [20][21]). A time varying voltage difference is applied across the electrodes. If the electric field (which is the spatial gradient of the voltage) at the vicinity of one of the electrodes exceeds a certain threshold, an ionization wave (a.k.a. streamer) propagates from that end to the other. A quasi-neutral plasma of a density proportional to the streamer velocity is left in its wake. Once the streamer bridges the gap, the plasma channel behaves as a conductor whose conductivity is determined by electron growth and decay processes whose rates are in turn determined by the applied voltage. The applied voltage is determined by the properties of the transmission line connecting the voltage source to the electrodes.

Each of the above steps can be modeled by invoking certain reasonable assumptions and are elaborated in the following sections.

2.1. Streamer Breakdown

Streamer breakdown refers to the process that gives rise to a streamer. For large gaps, it can occur far away from the electrodes (as per Meek's criterion [22]), but for short gaps it is determined by electron avalanches in the vicinity of the electrodes [21]. Since most SI applications involve small gaps, the latter model will be adopted to describe breakdown.

The breakdown voltage V_b for a given *plane* spark gap of length d at a pressure P, for a given gas, can be read from a so called *Paschen* curve. The curve describes the following breakdown condition [20]:

$$\alpha d = ln\left(1 + \frac{1}{\gamma}\right) \tag{1}$$

where α is the *effective* Townsend ionization coefficient, a property of the gas, and γ is the secondary ionization coefficient, a property of the electrode. α is an increasing function of the ratio of the electric field E to the number density N (i.e. the reduced electric field E/N), so the above equation implies that for a high enough pressure, the higher the electric field the smaller the gap length required to achieve breakdown.

α can be computed once the electron energy distribution function is known. Since this energy distribution is far from Maxwellian, owing to the long equilibration timescales of electrons subject to an external electric field, it must be computed by solving the Boltzmann transport equation [23]. BOLSIG+ is a numerical solver that does just this [24]. It also computes kinetic parameters (like α, electron mobility μ, ionization frequency ν, electron temperature T_e, etc.) by accounting for various collision processes that can occur in a non-equilibrium plasma. The scattering cross-sections for these processes can be found in LXCAT [25]. For the present work, the Phelps database [26] of scattering cross-sections is fed as an input to BOLSIG+, which outputs various kinetic parameters as functions of E/N.

Using kinetic parameters calculated via BOLSIG+, a Paschen curve can be plotted parametrically. Note that for a plane gap, voltage is trivially related to the electric field:

$$V_b = \frac{E}{N} N d \tag{2}$$

Eq. 1 can be rewritten with Nd on the left hand side like so:

$$Nd = \frac{ln\left(1+\frac{1}{\gamma}\right)}{\alpha/N} \tag{3}$$

Substituting for Nd in Eq. 3 from Eq. 2:

$$V_b = \frac{E/N}{\alpha/N} ln\left(1+\frac{1}{\gamma}\right) \tag{4}$$

If P is the pressure, and k is Boltzmann's constant, the ideal gas law $P = NkT$ furnishes a second relation from Eq. 3:

$$\frac{Pd}{T} = k\frac{ln\left(1+\frac{1}{\gamma}\right)}{\alpha/N} \tag{5}$$

V_b (Eq. 4) can thus be plotted against Pd/T (Eq. 5) by varying E/N from 0 to ∞ (i.e. a large number) for a fixed value of γ. This produces the desired Paschen curve but its parametric description is still cumbersome for use in a numerical code. It is better to approximate V_b as some *explicit* function of Pd/T. In this work, Chebyshev polynomials are frequently used to approximate such curves due to their spectral-like accuracy [27]. The Chebyshev polynomials $T_n(x)$ can be generated recursively as follows:

$$T_n(x) = \begin{cases} 0 & \text{for } n = 0 \\ x & \text{for } n = 1 \\ 2xT_{n-1}(x) - T_{n-2}(x) & \text{for } n > 1 \end{cases} \tag{6}$$

The Levenberg-Marquardt algorithm (LMA) [28], invoked from gnuplot [29], is used to fit the following polynomial to the exact Paschen curve:

$$V_b(x) = a_0T_0(x)+a_1T_1(x)+a_2T_2\left(\frac{1}{x}\right)+a_3T_3\left(\frac{1}{x}\right)+a_4T_4\left(\frac{1}{x}\right)+a_5T_5\left(\frac{1}{x}\right) \quad (7)$$

where $x = Pd/T$. Note the appearance of the reciprocal of x: this is to achieve the necessary bending behavior of the Paschen curve at small values of x. The appendix contains the values of all coefficients for this and all other fits. γ is fixed at 10^{-2}. Fig. 1 shows good agreement for the range of Pd/T values relevant for engines: at 1 atm, 300 K, and 1 mm gap length, $Pd/T = 0.337$, which is much greater than the value at which V_b attains its minimum and where the error in the fit is the largest.

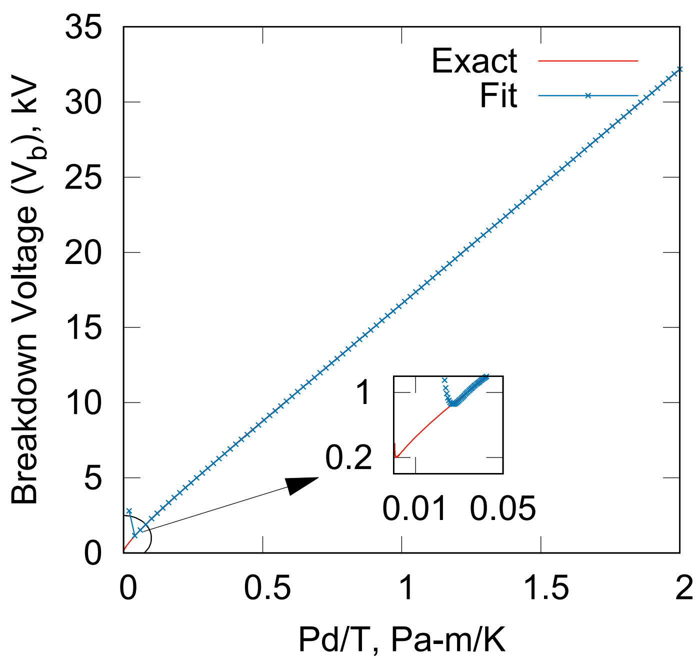

Figure 1. The exact Paschen curve for air computed using BOLSIG+, and its corresponding fit via Eq. 7. γ is set to 10^{-2}.

Of course, electrodes in SI engines are not planar and possess high curvature, but the breakdown voltage nevertheless scales with pressure in a Paschen-like fashion [6], i.e. the breakdown voltage always increases with pressure and decreases with gap length. Therefore, it remains possible to model the actual streamer breakdown voltage as $V_s = \psi V_b$ where ψ is some factor, typically less than unity, that accounts for the curvature of the electrodes. Higher the curvature, higher the local electric field and thus lower the value of ψ. ψ can be determined either numerically (via codes such as VizGlow [30] or AFIVO-Streamer [31]) or experimentally.

2.2. Streamer velocity and plasma density

Once V_s is achieved across the electrodes, a streamer propagates from anode to cathode, a fact that has been confirmed by both experiments and simulations for small gaps in air [21]. The speed of a streamer is directly related to the electric field E_m at its *head*. The higher its speed, the greater the ionization rate, and therefore the greater the plasma density n_m in the streamer's head and the greater the plasma density n_c in its wake. Simple closed relations between E_m, n_c, n_m, and the streamer velocity v_s can be derived by making certain reasonable assumptions regarding the manner in which the electric field decays in a steadily propagating streamer's head. The following formulae summarize these relations:

$$f = \frac{2\epsilon_0 \nu_m}{(2k' - 1)e^- \mu_{em}} \tag{8}$$

$$n_m = n_0 e^{W_0(f)} \tag{9}$$

$$n_c = n_m + \frac{\nu_m \epsilon_0}{e^- \mu_{em} k'} \tag{10}$$

$$v_s = \frac{e^- \mu_{em} n_c r_m}{2\epsilon_0 ln(n_m/n_0)} \tag{11}$$

Here, ϵ_0 is the permittivity of free space, ν_m is the ionization frequency at the streamer head, k' is the exponent in the power law relating the ionization frequency to that at the streamer head (i.e. $\nu = \nu_m(E/E_m)^{k'}$), e^- is the charge of an electron, μ_{em} is the electron mobility at the streamer head, n_0 is the initial plasma density, $W_0(f)$ refers to the Lambert function of f (i.e. $W_0(f)$ is the *real number* solution y to the equation $ye^y = f$), and r_m is the radius of the streamer. Note that the subscript m indicates that the properties are evaluated at the streamer head i.e. where $E = E_m$. n_0 can be set to the value of electron density due to cosmic rays ($10^9\ m^{-3}$) [20].

The following polynomial is used to fit n_c and v_s as a function of $x = E_m/N$ (for air) via LMA:

$$F(x) = \sum_{i=0}^{5} a_i T_i(x) \tag{12}$$

k' is set as 2.5. The pressure and temperature effects on n_c and v_s are taken into account via the following approximations:

$$n_c = F_{n_c}(E_m/N) \times \left(\frac{P}{P_{ref}}\frac{T_{ref}}{T}\right)^2 \tag{13}$$

$$v_s = F_{v_s}(E_m/N) \times \left(\frac{r_m}{r_{m,ref}}\right) \times \left(\frac{P}{P_{ref}}\frac{T_{ref}}{T}\right)^{0.935} \tag{14}$$

Here, $P_{ref} = 1\ atm$, $T_{ref} = 300\ K$, and $r_{m,ref} = 10^{-3} m$. Eqs. 13 and 14 indicate that the role of N is not restricted to the reduced electric field E_m/N but also appears as an additional power law dependency. This can be appreciated from Figures 2 and 3.

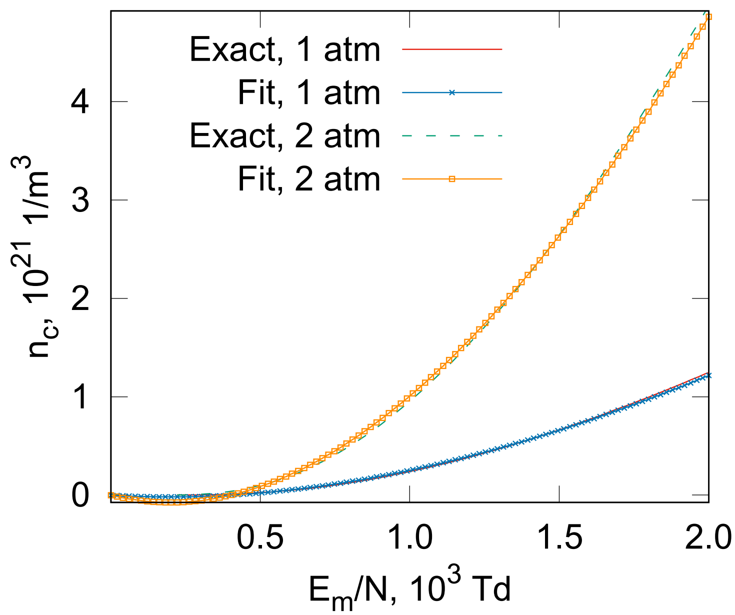

Figure 2. The plasma density n_c in the wake of a streamer propagating in air as a function of E/N. Both exact and fit functions are shown for two pressures keeping temperature fixed at 300 K.

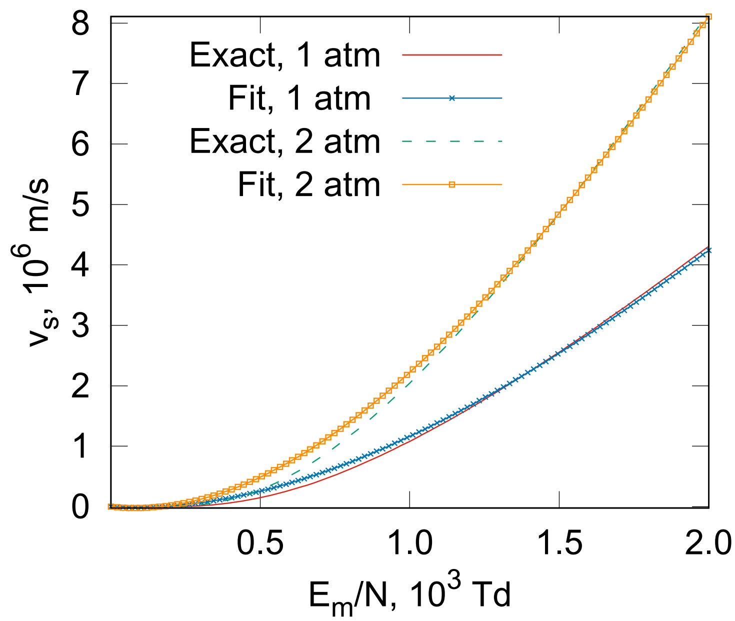

Figure 3. The streamer velocity v_s in air as a function of E/N. Both exact and fit functions are shown for two pressures keeping temperature fixed at 300 K and r_m fixed at $10^{-3}m$.

The free parameters are thus E_m and r_m, both of which can be estimated from experiments or detailed simulations. Recent progress has been made in measuring the electric field in ionization waves, albeit at low pressures [32]. Simulations have shown that both E_m and r_m change (typically increase) with time [33], so suitable time-averaged values must be chosen for the simulations. A more sophisticated model would take into account the rate of change of r_m, but for the present study, r_m is kept fixed over the course of a discharge simulation. Sensitivity of energy delivery to r_m is presented in the Results section.

2.3. Plasma density evolution

Once the streamer bridges the gap, the plasma density is *initialized* at n_c for the entire gap except for an extremely thin region (i.e. the cathode fall) located at the cathode. This n_c changes principally due to ionization, attachment, and recombination reactions. The bulk evolution of electron density n_e is thus given by

$$\frac{dn_e}{dt} = (\nu - b)n_e \tag{15}$$

where ν is the *effective* ionization frequency (with the attachment frequency subtracted out, both calculated via BOLSIG+) and b is the recombination frequency, with n_c as the initial condition for the above differential equation.

ν is given by the following fit where $x = E/N$:

$$\nu(x)/N = \sum_{i=0}^{5} a_i T_i(x) \tag{16}$$

Note from Fig. 4 that there exists a range where ν is negative, due to the attachment coefficient being subtracted out. The fit over-estimates this negativity, but was not found to affect the simulations because electron recombination typically dominates where ionization doesn't.

Since a key emphasis in this work is to understand the scaling of discharge processes with pressure, it is necessary to account for both two-body and three-body electron recombination processes. b is thus given by [34] a sum of these processes as follows:

$$b = b_1 + b_2 + b_3 \tag{17}$$

$$b_1 = 2.8 \times 10^{-13}\sqrt{\frac{300}{T_e}} \tag{18}$$

$$b_2 = 1.4 \times 10^{-41}\left(\frac{300}{T_e}\right) e^{(-600/T)} e^{(700(T_e-T)/TeT)} N_{O_2}^2 \tag{19}$$

$$b_3 = 1.07 \times 10^{-43}\left(\frac{300}{T_e}\right)^2 e^{(-70/T)} e^{(1500(T_e-T)/TeT)} N_{O_2} N_{N_{N_2}} \tag{20}$$

where b_1 is due to two-body recombination, b_2 and b_3 are due to three-body recombination, T_e is the electron temperature in Kelvins (calculable from BOLSIG+ for a given E/N), T is the gas temperature in Kelvins, N_{O_2} is the number density (in

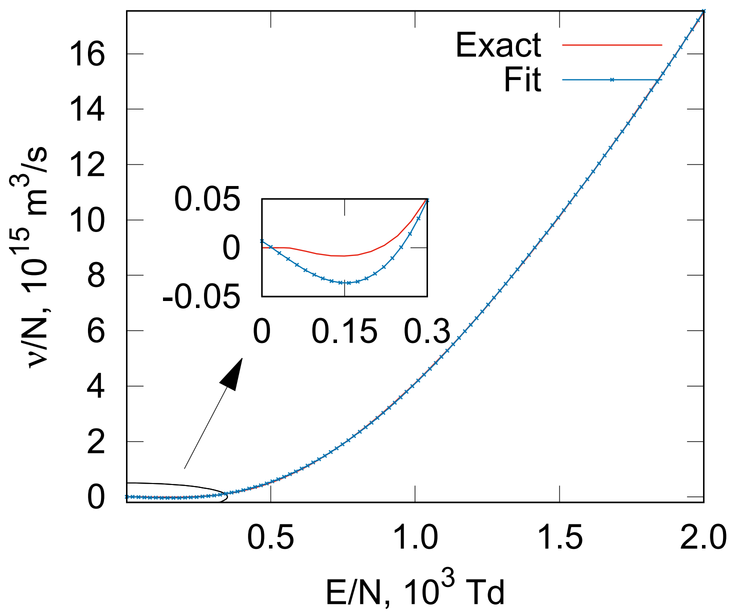

Figure 4. The *effective* ionization frequency ν in air computed using BOLSIG+, and its corresponding fit via Eq. 16. Note that the attachment frequency is subtracted out leading to a region where ν is negative.

$1/m^3$) of oxygen, and N_{N_2} is the number density of nitrogen. The coefficients appearing in the above expressions ensure that the unit of b is $1/s$.

It is well known that the plasma density evolution dramatically changes when the discharge transitions to a spark, occurring chiefly due to hydrodynamic phenomena [35] and/or electron detachment processes [36]. More recent work by Pai et al. has clarified many aspects of the transition process, particularly the distinction between hydrodynamic purely kinetic influences[37]. The present study is limited to cases where energy is not applied over a time scale long enough for hydrodynamic phenomena to couple with the discharge. Electron detachment processes can be taken into account with a more complex kinetic model, but for the purpose of illustration, this aspect is ignored in the present model. The current attainable in such discharges can nevertheless be *spark like* i.e. $\sim$ 10 A (see Results section).

2.4. Radical production

Although not directly coupled to the energy delivery from the circuit to the gas, it is nonetheless useful to keep track of certain chemical species formed, especially for diagnostic purposes relating to ignition [38]. In this section, the production of oxygen radicals (O) is dealt with briefly. Other minor chemical species are expected to behave similarly.

The rate of an inelastic electron collision reaction can be obtained from the electron energy distribution and collision cross-section for the particular reaction, much like ionization and attachment reactions in the previous section. O radical formation follows from the rapid dissociation of an electronically excited O_2 molecule at 6.12 eV. The rate coefficient of this reaction is shown in Fig. 5 and is fit to the following expression (where $x = E/N$):

$$k_O(x) = a_0 e^{\left(\frac{a_1}{x} + a_2 log(x) + a_3 log(x)^2\right)} \tag{21}$$

The leading term resembles the Arrhenius form, and the logarithmic terms provide necessary perturbations to improve the fit to the data. The reason for using such an expression is the strict requirement for the rate to go to zero as $E/N \to 0$, which isn't always possible for Chebyshev polynomials due to oscillations near the end points of the provided data. Such expressions seem to have first been used by Janev et al.[39].

As pointed out by Rusterholtz et al.[40] and others, a more important channel for O production is due to the collisional deactivation of excited the excited nitrogen state (7.35 eV) $N_2(B)$ which is known to occur at a rate of $3 \times 10^{-16} m^3/s$. The formation of $N_2(B)$ by electron impact is also given by fit similar to 21 and these are shown in Fig. 5.

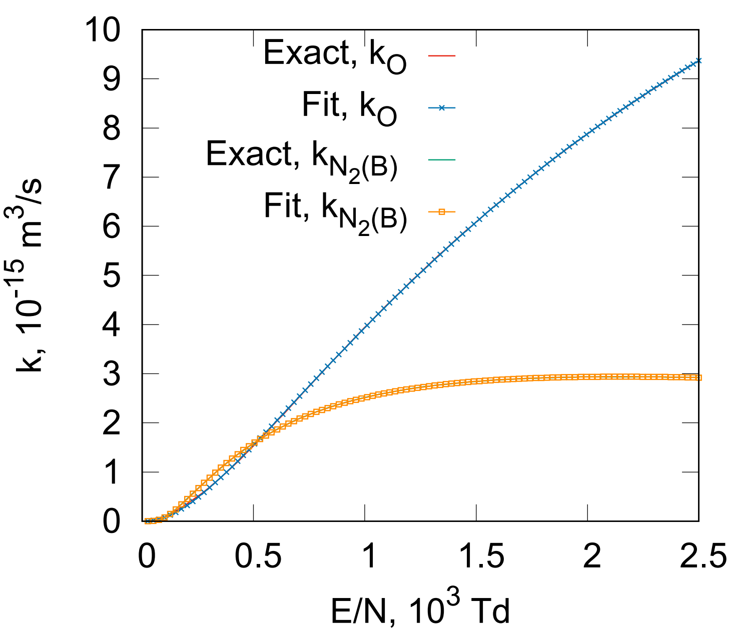

Figure 5. The rate coefficients for the formation of $O_2(6.12\ eV)$ and $N_2(B)$ (7.35 eV) due to electron collisions computed using BOLSIG+, and its corresponding fit via Eq. 21 .

The concentration of O radicals produced at the streamer head can also be approximated as follows. From a frame of reference attached to the streamer head, the total amount of O radicals formed is given by:

$$[O]_s \approx \frac{\int_{-\infty}^{\infty} 2k_O[O_2]n_e dx}{v_s} \tag{22}$$

where $[O_2]$ is the oxygen number density and the integral covers the entire streamer. Equations like Eq. 22 are widely used in the combustion community to determine flame speeds [41]. If we assume that the production is contained within a thin region where the field is E_m, we have

$$[O]_s = \frac{2k_O(E_m)[O_2]n_m\Delta x}{v_s} \tag{23}$$

where $\Delta x \approx r_m n_m/n_c$ is the streamer head thickness. Note that since the streamer velocity is directly proportional to the streamer head radius r_m, $[O]_s$ is independent of r_m, much like n_m and n_c. The following polynomial is used to fit O_s as a function of $x = E_m/N$:

$$F_O(x) = \sum_{i=0}^{5} a_i T_i(x) \tag{24}$$

The pressure and temperature effects are taken into account via the following approximation:

$$[O]_s = F_o(E_m/N) \times \left(\frac{P}{P_{ref}}\frac{T_{ref}}{T}\right)^{1.93} \tag{25}$$

As seen from Fig. 6, the fit is satisfactory. $[O]_s$ serves as the initial condition in the evolution of O radicals once the streamer bridges the gap, just like n_e in the previous section. Similar considerations apply to $N_2(B)$ and other such species produced in the streamer head.

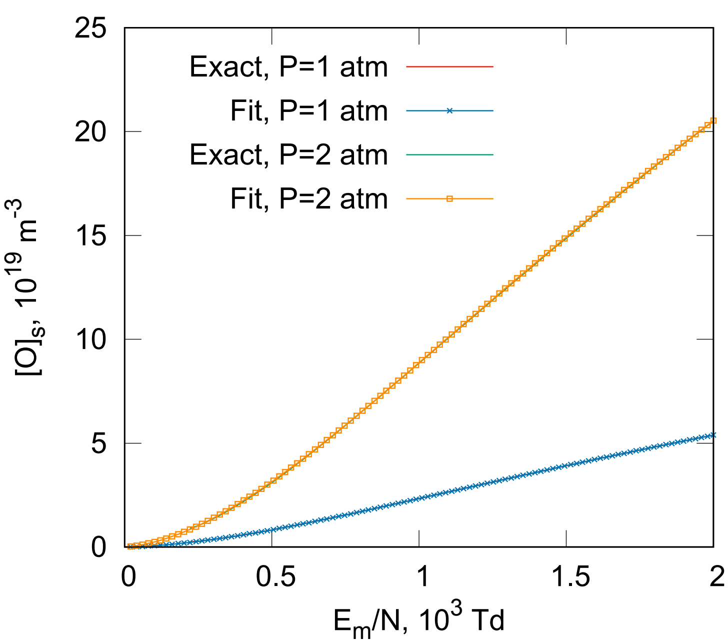

Figure 6. The concentration of O radicals in the wake of a streamer computed using Eq. 23, and its corresponding fit Eq. 25 .

2.5. Cathode Fall

Once the streamer bridges the gap, electrical boundary layers form at both electrodes and are termed the anode fall at the positive end and the cathode fall at the negative end [20]. The anode fall is accompanied by a much smaller voltage drop compared to the cathode fall and will thus be neglected here. The voltage drop due to the cathode fall is important to consider because it modifies the electric field in the bulk of the plasma, i.e. if V is the voltage across the electrodes, and V_c is the cathode fall voltage, the electric field in the quasi-neutral plasma of density n_e (whose evolution is determined by Eq. 15) is given by $E = (V - V_c)/d$, neglecting the extremely small thickness of the cathode fall layer (typically of the order of a Debye length). Since the ionization, decay, and mobility of electrons are strong functions of E/N, the role of V_c is therefore significant.

The cathode fall voltage V_c is related to the cathode fall current density j_c parametrically via the reduced gap length $d' = Pd/(Pd)_n$ [20]:

$$\frac{V_c}{V_n} = \frac{d'}{1 + log(d')} \tag{26}$$

$$\frac{j_c}{j_n} = \frac{1}{d'(1 + log(d'))^2} \tag{27}$$

where V_n is the *normal* cathode fall voltage and is related to the minimum voltage of the Paschen curve via $V_n = 1.1V_{min}$ and j_n is the corresponding *normal* current density given by

$$j_n = \frac{P^2(1+\gamma)\mu_p V_n^2 \epsilon_0}{4\pi(Pd)_n^3} \tag{28}$$

where $\mu_p \approx 20m^2Pa/V/s$, and $(Pd)_n = 1.4(Pd)_{min}$ where $(Pd)_{min}$ is the value of Pd corresponding to the minimum voltage on a Paschen curve. The cathode fall voltage is plotted against current density in Fig. 7. It can be seen that for $j/j_n < 1$, V_c/V_n rises, so this portion of the curve is deemed unphysical and in simulations V_c/V_n is set to unity in this range.

The algorithm for solving for V_c at every instant is as follows:

(i) Given a circuit current I, the current density j_c is $I/(\pi r_m^2)$.

(ii) Now that j_c is known, d' can be calculated from Eq. 27. A non-linear root finding method (like Brent's [42]) is required for this step and care must be taken to extract only the root that corresponds to $1/e < d' < 1$ as another root lies very close for large values of j/j_n as seen in Fig. 7.

(iii) With d' thus found, V_c can be calculated from Eq. 26.

2.6. Circuit current

The circuit current I arises first due to the propagation of the streamer (of velocity v_s given by Eq. 14), which upon idealizing as a perfect cylindrical conductor generating

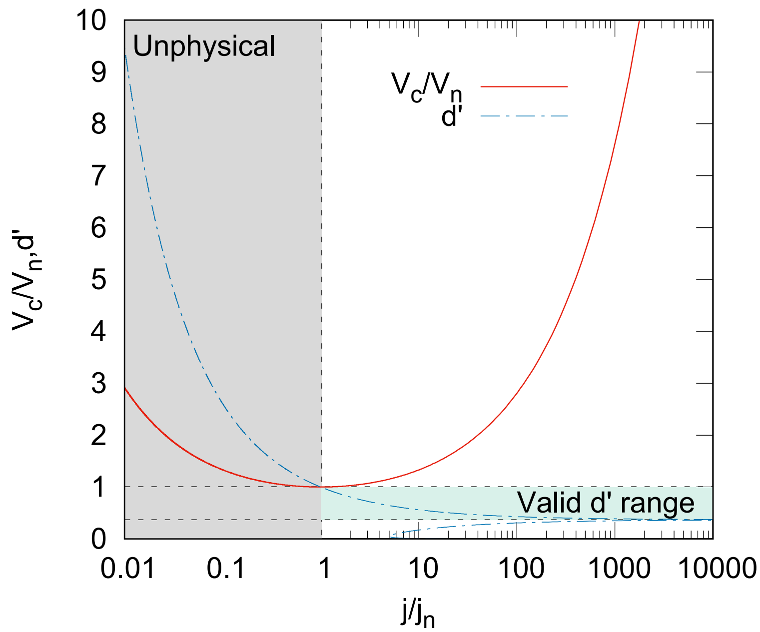

Figure 7. The dimensionless cathode fall voltage V_c/V_n and dimensionless gap length d' as functions of the dimensionless current density j/j_n. The region $j/j_n < 1$ corresponds to an abnormal fall region where the voltage rises with current and is unphysical. The solution to Eq. 27 must be limited to the range $1/e < d' < 1$, which is also shown.

charge in its wake, can be given as [21]

$$I = \frac{l}{l + r_a} \frac{2\pi\epsilon_0 V v_s}{log(l/r_m)} \tag{29}$$

where l is the length of the streamer (evolving according to $dl/dt = v_s$), r_a is the radius of the anode, and V is the voltage applied across the electrodes. The appearance of r_a is due to charge accumulation at the electrode tip. Eq. 29 is derived using the Shockley-Ramo theorem which relates the current to that of a moving charge in the vicinity of an electrode [43].

Once the streamer bridges the gap, the current I due to the flow of electrons in the plasma is given by Ohm's law i.e. $I = (V - V_c)/R'$ where

$$R' = \frac{d}{\pi r_m^2} \frac{1}{e^- n_e \mu_e} \tag{30}$$

μ_e is given by the following fit for air:

$$\mu_e(x)N = \frac{a_0}{log(x + a_1)} \tag{31}$$

The fit is shown in Fig. 8.

In addition to the flow of electrons through the plasma, the time variation of electric field produces a *displacement* current which must be added to the above [44]. This is

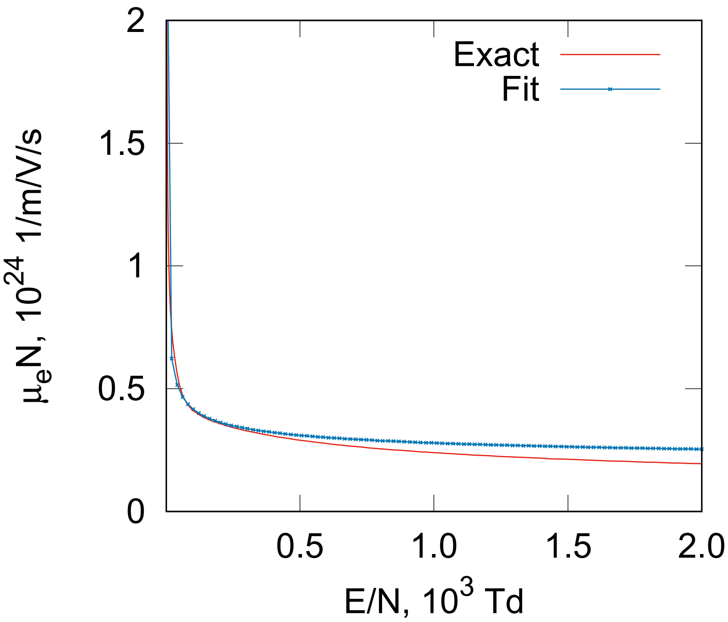

Figure 8. The electron mobility in air computed using BOLSIG+ and its corresponding fit via Eq. 31.

given by CdV/dt where C is the capacitance of the electrodes and is only a geometric property of the system. For typical spark plugs, this can range from tens to hundreds of pico-Farads.

2.7. Transmission Line

The voltage across the electrodes is rarely ever the voltage applied at the source. Voltage drops occur in different parts of the underlying circuit, thus modifying the voltage and current across the discharge and more importantly the energy delivered there. For nanosecond pulsed discharges, an impedance mismatch between the source and discharge can can cause additional losses: a voltage pulse submitted at the source is subject to *transmission* and *reflection* at the electrodes [45] and this needs to be accounted for when evaluating the performance of the discharge. The voltage pulse at the electrodes is also *delayed* by a time τ due to the finite propagation time of an electromagnetic disturbance through the connecting cable. For a lossy transmission line, the telegraph equations must be solved at every instant to determine the voltage across the electrodes [46]. For lossless transmission lines however, the telegraph equations can be solved *apriori* via the method of characteristics to yield a direct relationship between the voltage at the electrodes and the source [47]. If I_s is the current from the source, and V_s the accompanying voltage, the current I_e and the voltage V_e at the opposite end of the transmission line of characteristic impedance Z_0 and time delay τ are connected via the following relations:

$$I_s = (V_s - E_i)/Z_0 \tag{32}$$

$$I_e = (V_e - E_r)/Z_0 \tag{33}$$

$$E_i = 2D(V_e, \tau) - D(E_r, \tau) \tag{34}$$

$$E_r = 2D(V_s, \tau) - D(E_i, \tau) \tag{35}$$

Here D is the delay operator and is defined as:

$$D(y, \tau) = \begin{cases} y(t-\tau) & \text{for } t > t_s + \tau \\ y(t_s) & \text{for } t < t_s + \tau \end{cases} \tag{36}$$

where t_s is the simulation start time.

Eq. 33 connecting the electrode side current and voltage must be simultaneously solved along with the current-voltage relationships mentioned in the previous section in order to close the system of equations.

3. Computational approach

The various building blocks of the previous section need to be stitched together and this job is greatly facilitated by the Object Oriented Modeling language *Modelica* [48]. Each block (object) houses its instruction set in the form of its governing differential-algebraic equations alongside its parameters, all handled *symbolically* i.e. using computer algebra [49]. The blocks are then combined in a network, which in the current context is an electrical circuit. The rules for the connections are automatically handled according to the type of problem being solved. For the present *electrical* problem currents are summed to zero at junctions and voltage differences are summed to zero along a loop. In other words, Kirchhoff's laws are used to generate the necessary algebraic constraints to close the total system of equations. The entire set of equations is then translated from symbols to a numerical implementation compiled in C. This generated binary contains the necessary rate of change of the solution vector y, comprising the voltage, current, streamer length, power dissipated, etc. Any time integrator can then be selected to integrate the system of equations for given initial conditions and parameters. For the present study, where transmission lines are not involved, IDA [50] is used, otherwise a fourth order Runge-Kutta method [51] is used. The choice of the latter is due to numerical difficulties encountered in the formulation of the system Jacobian in the presence of the delay operator (Eq. 36), the investigation of which is beyond the scope of the present work.

The implementation of Modelica used for the present study is *Open Modelica* [52] and its key advantages are that

(i) modular coding is baked into its use, making documentation and unit testing *nearly* implicit

(ii) objects can be connected, manipulated, and navigated *graphically*

(iii) most attractively, its Functional Mockup Interface (FMU) allows other solvers to interact with its binaries, thus making the model straightforwardly usable in other codes.

4. Results and Discussion

4.1. Circuit without a transmission line

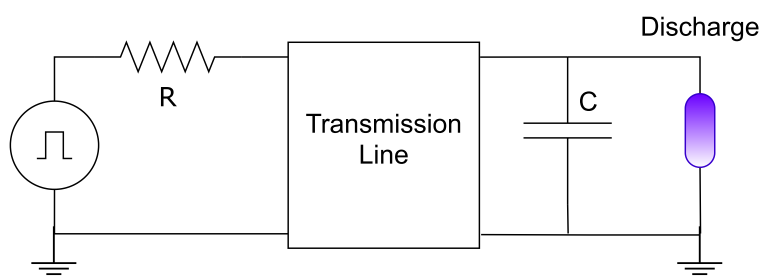

Figure 9. A circuit showing the connection between the voltage source and the discharge.

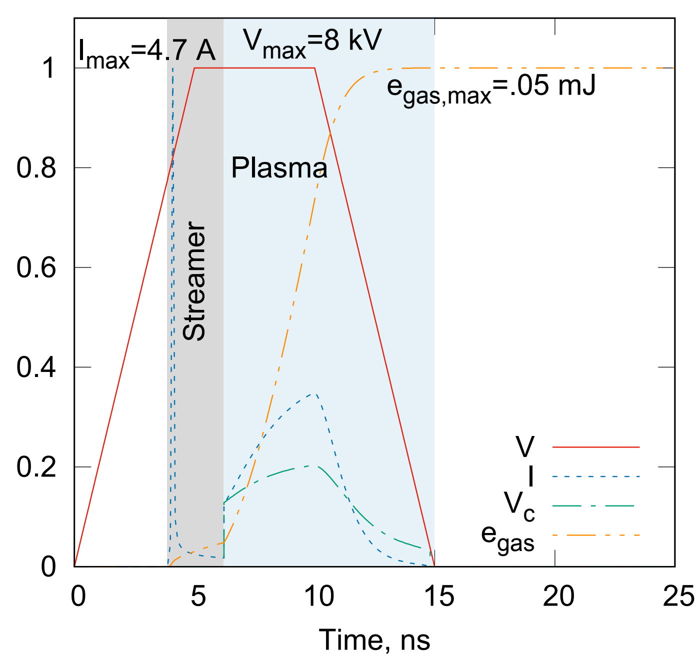

Figure 10. A typical circuit output for an LTP discharge in air between two closely spaced electrodes upon application of a trapezoidal voltage pulse. Here $P = 1\ atm$, $T = 300\ K$, $d = 1\ mm$, $r_m = 0.1\ mm$, $E_m = 2000\ Td$. Voltage, current, and e_{loss} are normalized by their maxima V_{max}, I_{max}, and $e_{gas,max}$ respectively. V_c is normalized by V_{max}.

The full circuit is shown in Fig. 9. Before discussing the effects of the transmission line on the discharge, it is instructive to first run simulations in its absence. Removing the upstream resistance R and fixing the capacitance C as 30 pF, a trapezoidal pulse of 5 ns rise time, 5 ns fall time, and 5 ns width is applied across the electrodes. ψ is set to unity, and the gap width to 1 mm, and so at 1 atm and 300 K, the streamer breakdown voltage $V_s = 6.194\ kV$. The anode radius r_m is set to 0.01 mm. This set of parameter values will be referred to as *standard conditions* henceforth. All parametric variations are carried out in the vicinity of these conditions. Fig. 10 summarizes a typical response.

It is observed that when V_s is reached, a streamer is formed ($\approx 3.8\ ns$) and quickly bridges the gap. Since the discharge is subjected to a non-zero voltage just after this, ionization and attachment reactions occur *in* the plasma, adjusting its resistance and therefore the current flowing through the circuit. The flow of current also gives rise to the cathode fall voltage, whose maximum is observed to reach $\approx 0.2V_{max}$ and plays a crucial role in limiting the reduced electric field E/N in the gap: without the cathode fall voltage, the current reached is at least an order of magnitude higher. Fig. 10 also shows that the current changes discontinuously between the streamer and plasma phases. This is admittedly a shortcoming of the model: the physics in the short time between the streamer bridging the gap and the electron density evolution of the homogenized plasma is neglected. It is expected however, that this does not affect the results significantly due to its extremely short duration.

The energy deposited in the gas, e_{gas} (which is simply the time integral of the product of voltage across the discharge and the current flowing through it) is also shown in Fig. 10. It is seen that most of the energy is deposited *after* the streamer bridges the gap. This trend is qualitatively similar to that reported by Rusterholtz et al. [40]: there, the energy delivered is much higher because the initial gas temperature (1000 K) is much higher than that used here. The high temperature, all else being equal, increases E/N which increases the ionization which increases the current. Indeed, the present model furnishes much closer values for e_gas (0.4 mJ) to Rusterholtz et al.'s value (0.6 mJ) when this change in temperature alone is made.

e_{gas} is an important quantity for diagnostics as it directly relates to the maximum temperature attainable and the concentrations of various chemical species of interest. It is well known that in non-equilibrium discharges, much of the energy delivered to the gas is expended on inelastic collisions: in fact this is their most attractive feature. Fig. 11 shows the fraction of delivered energy that activates inelastic collisions compared to the fraction that activates ionization (or growth) processes. For low enough electric fields, inelastic processes dominate, so it is prudent to ensure that fields attained in the plasma are not too high.

Since the radius of the streamer r_m is a parameter in this model, it can be varied to understand how the energy delivered to the gas depends on it. Fig. 12 shows that although the delivered energy increases with r_m, the energy *density* (calculated by dividing the e_{gas} by the volume of the discharge $\pi r_m^2 d$) asymptotes. This is because at

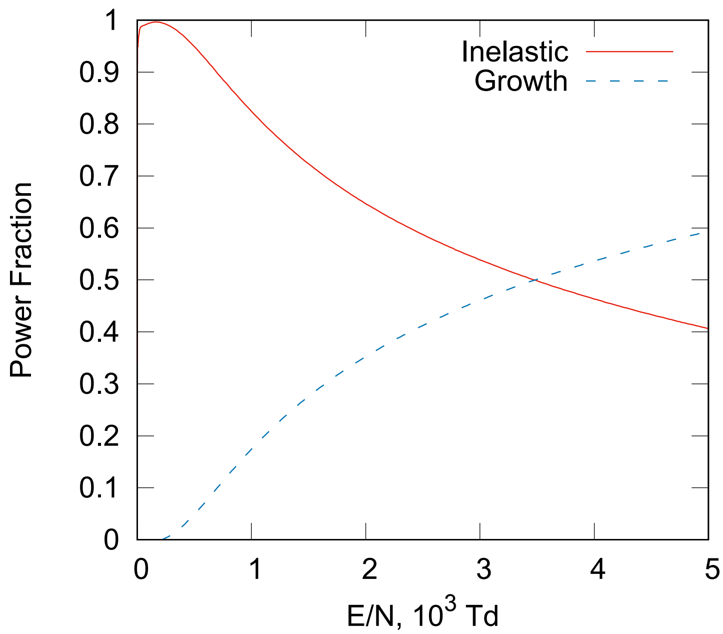

Figure 11. The fraction of energy (or power) that goes to inelastic collisions and ionization (or growth) collisions as a function of E/N computed via BOLSIG+.

small r_m, the current density and therefore the cathode voltage fall V_c are very high, making the effective E/N in the discharge low and consequently the ionization low. At high enough r_m, the cathode voltage fall is small enough that it does not impede ionization.

Another parameter in the model is the reduced field in the streamer head E_m/N and its effect on the delivered energy can also be examined, as shown in Fig. 13. It is observed that the energy density delivered increases with E_m/N. This is due to the fact that the electron density in the wake of the streamer n_c is higher for higher E_m/N, as per Fig. 2. For larger radii, the energy delivered increases faster with E_m/N due to the streamer current's direct dependence on the streamer radius (via the streamer velocity given by Eq. 11).

The effect of the pulse rise time τ_r, fall time τ_f, and width τ_w on the energy delivered is shown in Fig. 14. It is observed that the pulse width has the greatest impact on the energy delivered, simply because it is during this period that the applied voltage is the maximum. During the pulse rise, energy is delivered to the gas only *after* breakdown, and during the pulse fall, the plasma resistance rapidly increases leading to a diminishing current.

The breakdown voltage is also a key determining factor in the amount of energy delivered and can be investigated by varying ψ. Fig. 15 shows an interesting non-monotonicity in the energy delivered as ψ increases. This is observable for both small and large streamer radii and can be explained by noting the evolution of E/N and n_e for different values of ψ, as is shown in Fig. 16. For $\psi = 0.1$ and $r_m = 0.1$ mm,

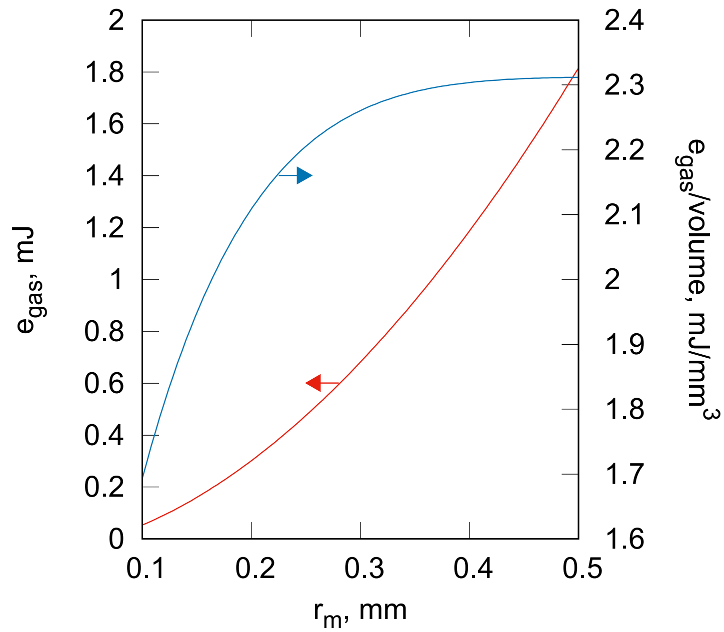

Figure 12. The variation of energy and the density of energy delivered to the gas with the streamer radius, at standard conditions.

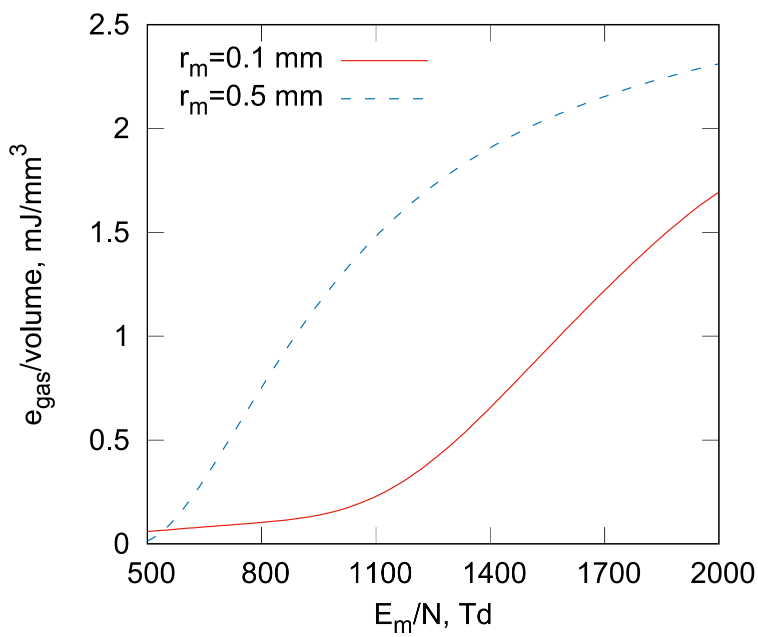

Figure 13. The density of delivered energy for a discharge at 1 atm, 300 K, and the trapezoidal pulse shown in Fig. 10.

the reduced electric field is so low after the streamer bridges the gap (the kink in E/N indicates when this occurs), that recombination dominates over ionization and n_e decreases before it increases. On the other hand, more of the rise time is available for

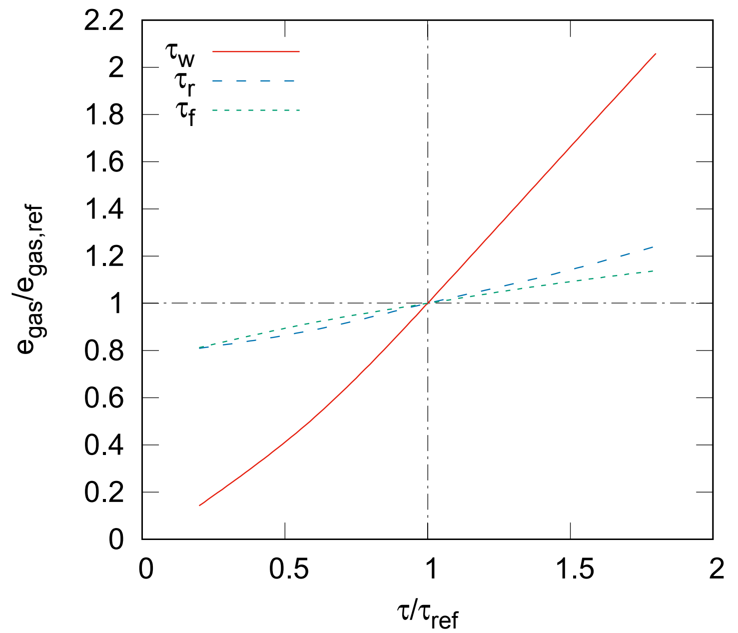

Figure 14. The energy delivered to the gas, scaled by that delivered at standard conditions $e_{gas,ref}$, shown as a function of scaled time τ/τ_{ref}. The three different curves correspond to the variation with pulse width τ_w, pulse rise τ_r, and pulse fall τ_f times.

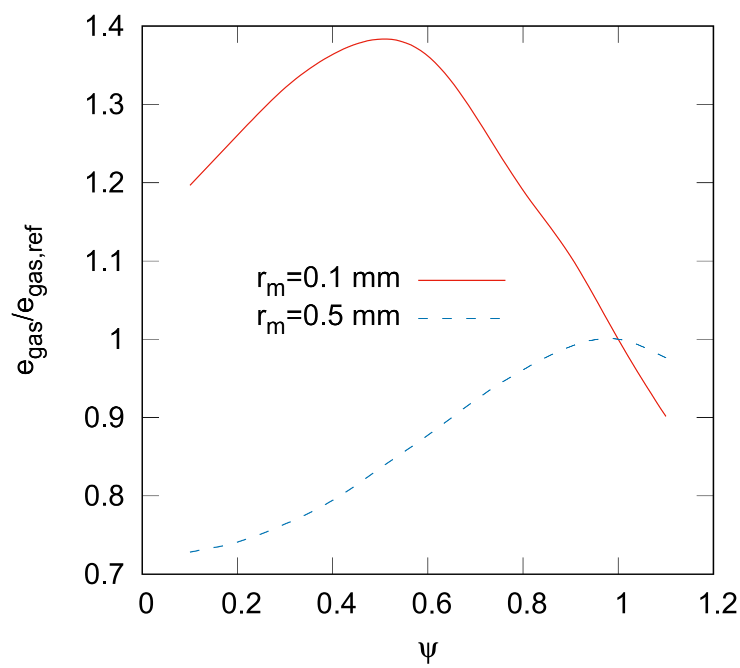

Figure 15. The energy delivered at standard conditions, scaled by that delivered when $\psi = 1$, for two different streamer radii.

energy deposition, since breakdown has occurred early. The overall effect of this is that the energy deposited is greater than the $\psi = 1$ case. When $\psi = 0.5$, breakdown occurs

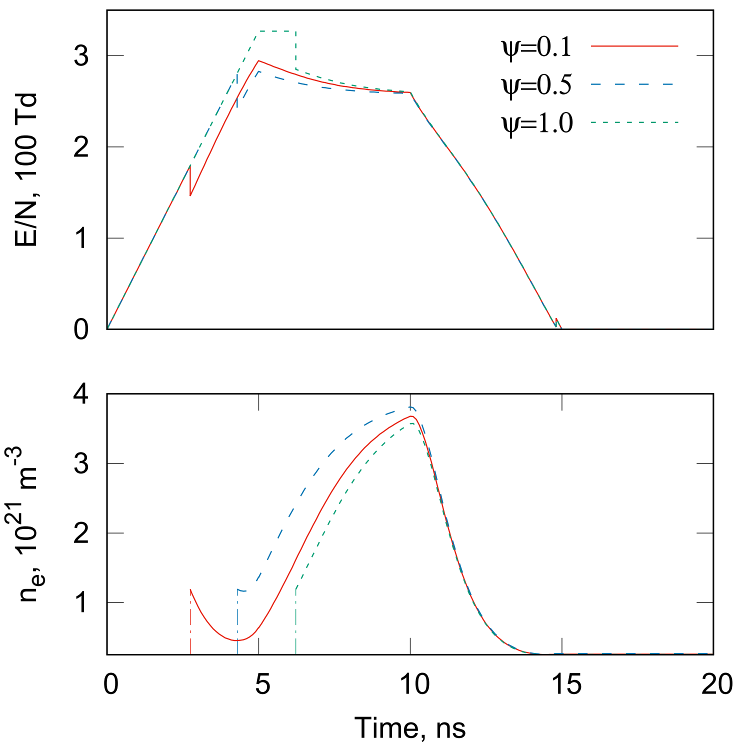

Figure 16. The evolution of the reduced electric field and electron density for three different values of ψ at $r_m = 0.1$ mm.

when E/N is high enough that ionization once again begins to dominate. This is why e_{gas} initially increases with increasing ψ.

For higher values of ψ, the breakdown occurs late enough that much of the energy is not delivered to the gas, so e_{gas} decreases with increase in ψ. For larger radii and small enough ψ, the streamer bridges the gap faster, leaving a longer duration of time over which recombination dominates ionization. This is why the curve in Fig. 15 shifts to the lower right for higher r_m.

4.2. Circuit with a transmission line

The inclusion of a transmission line adds to the richness of the aforementioned phenomena: the voltage applied is no longer the voltage across the electrodes, but one modified due to the impedance mismatch between the two ends of the line. Fig. 17 shows this effect in the presence and absence of a discharge. The line has a characteristic impedance of 50 Ω and a time delay of 25 ns. The trapezoidal pulse submitted at the source end of the line (labeled *in*) is seen to exit with nearly twice as high an amplitude when there is no discharge (labeled *out*); the time integration introduces limited numerical dissipation. This pulse travels back up the line and appears with a reduced amplitude due to the upstream resistance (fixed at 10 Ω), and this pulse once again travels down the line and appears with a negatively amplified voltage.

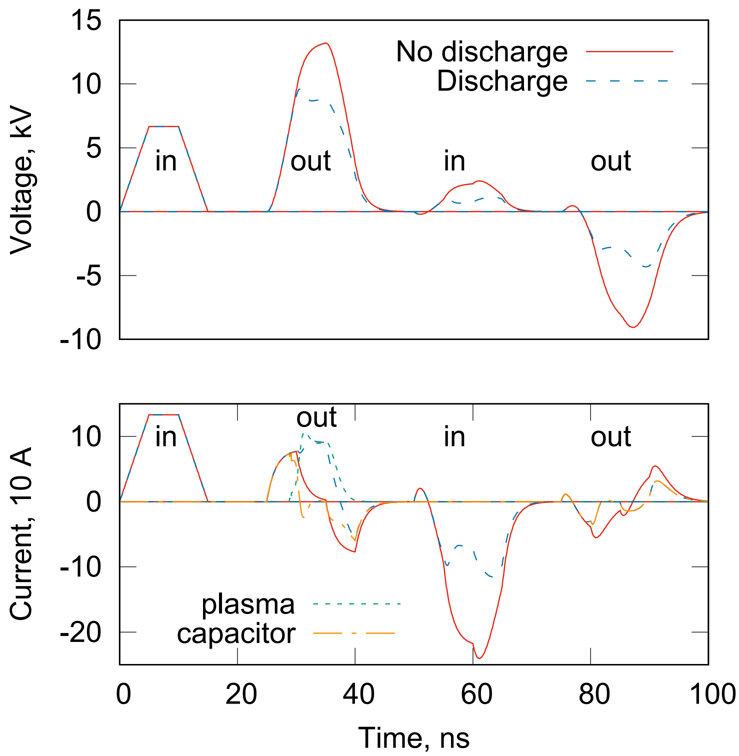

Figure 17. The voltage and current traces in the presence of a transmission line corresponding to standard conditions. Segments labeled *in* refer to the source side of the line and those labeled *out* refer to the discharge side. Circuit current due to plasma (including that due to streamer propagation) and the capacitor are shown.

Both the observed voltage and current follow the known behavior of transmission lines; the reader is referred to [45] for a thorough discussion of their behavior. When a discharge occurs, the voltage across it is diminished due to its dynamically changing impedance. The circuit current due to the discharge is also shown in Fig. 17: the capacitor first charges and then rapidly discharges once the breakdown voltage is reached, leading to a high plasma induced current. Upon reflection, the current turns negative and subsequent currents on the discharge side are entirely capacitive as the plasma has decayed and the voltage in subsequent reflections is too low to initiate breakdown. The scope of the present study is limited to the case of a single pulse.

The voltage across the discharge is higher than what is applied and is determined by the instantaneous impedance mismatch between the source and the discharge. This carries profound implications for the energy delivered. Repeating the parametric variation of r_m, as was done in Fig. 12, shows an opposite trend (seen in Fig. 18): increasing r_m is seen to *decrease* the density of energy delivered. Also, the ratio of the energy delivered to the gas to the energy submitted at the source (a.k.a. energy efficiency e_{gas}/e_{in}) is seen to asymptote at high values of r_m, indicating that the proportion of reflected energy diminishes to a constant for large r_m. Thus, high energy efficiency does not imply high energy loading, a significant trade-off to be met in the design of nanosecond pulsed systems.

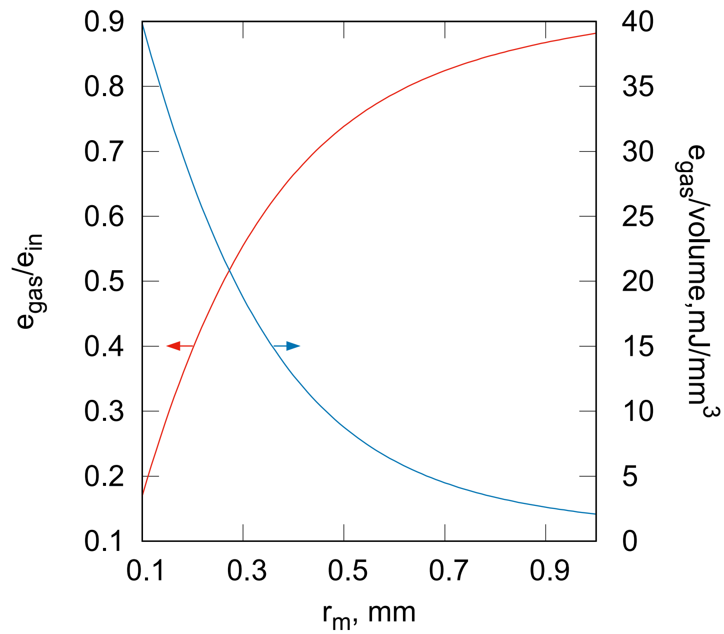

Figure 18. The variation of energy efficiency and the density of energy delivered to the gas with the streamer radius, at standard conditions, in the presence of a transmission line.

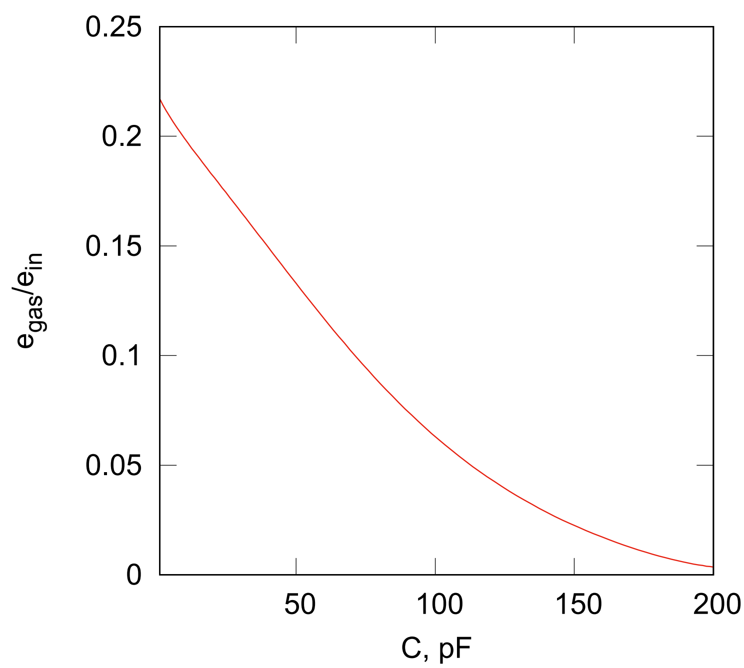

Figure 19. The energy efficiency variation with downstream capacitance, at standard conditions.

The energy that does not make it to the gas is reflected to the source and what determines the amount reflected is primarily the capacitance of the electrode system. Fig. 19 shows how the energy efficiency decreases with capacitance; the calculation shows that for this particular configuration, lower the capacitance, the better the energy efficiency. Such information is utilized in optimizing nanosecond pulsed discharge systems, as was done in [11]. The recent work of Balmelli et al. [53] shows the importance of taking such energy reflections into account when evaluating the performance of nanosecond pulsed igniters.

For SI engines, and for a given voltage pulse and transmission line, the energy loading and efficiency must be studied as a function of the compression in the cylinder. Isentropic compression relates the final temperature and number density of the gas to the pressure ratio P/P_0 via the adiabatic index γ (not to be confused with the secondary ionization coefficient):

$$T = \left(\frac{P}{P_0}\right)^{(\gamma-1)/\gamma} T_0 \tag{37}$$

$$N = \left(\frac{P}{P_0}\right)^{1/\gamma} N_0 \tag{38}$$

Therefore, the compression in the cylinder is seen to modify the pressure, temperature, and number density simultaneously, and each of these are expected to have an effect on the discharge, chiefly via the reduced electric fields E/N and E_m/N. Furthermore, the variation of the streamer radius with compression must also be taken into account. A simple scaling law is used here for this purpose [21]:

$$r_m = \frac{\alpha_0}{\alpha} r_{m,0} \tag{39}$$

where $r_{m,0}$ is the reference streamer radius at 1 atm and 300 K, α_0 is the Townsend ionization coefficient (defined as $\nu/(\mu_e EN)$ at these conditions at some reference E_m/N_0. r_m and α thus correspond to the *compressed* values calculated at P, T, and N. Such a scaling ensures that the streamer radius decreases with pressure. γ is held at a value of 1.4. To ensure that breakdown occurs across the entire range of pressures, a high enough voltage amplitude must be used. For the present study, 15 kV is chosen, with $r_{m,0} = 0.5$ mm.

Fig. 20 shows how the energy efficiency and loading vary with P/P_0. The energy efficiency monotonically decreases because the streamer radius decreases (due to the above scaling law), and the electron density decreases (due to the decreased E/N), both of which lead to an increase in the streamer resistance. The energy density however exhibits a non-monotonic trend: it first increases up to a certain pressure and then decreases. As pressure increases, the breakdown voltage increases, leaving a smaller duration for energy delivery. Higher pressure can compensate for decreased E/N to some extent (as is seen from Fig 2, 3, and 4), and this is why the energy loading first increases with pressure. Eventually, the effect of low E/N overwhelms the system so much that the energy loading rapidly decreases with pressure. A numerical experiment

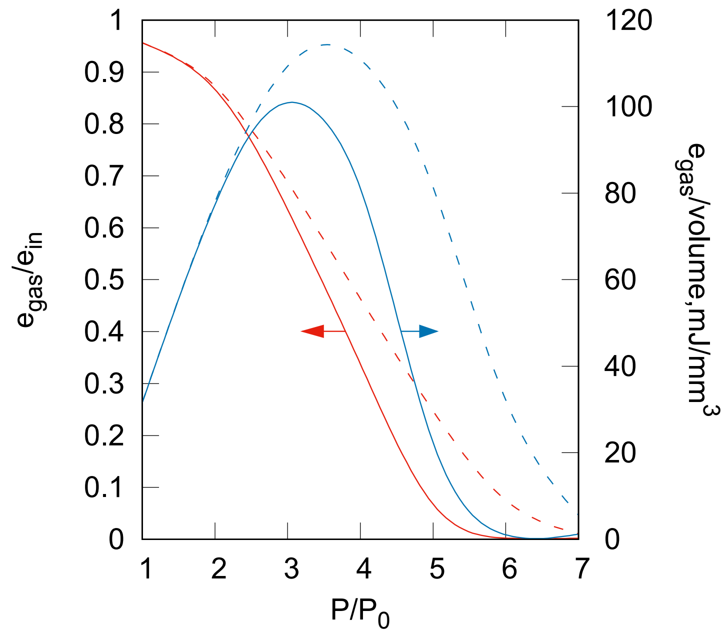

Figure 20. The energy efficiency and delivered energy density as a function of pressure in the presence of a transmission line. The dashed lines correspond to the case where E_m/N is fixed as E_m/N_0.

wherein E_m/N is fixed across the entire range of pressures was also conducted; the results are shown as dashed lines in Fig. 20, indicating that the falloff behavior persists, albeit at slightly higher pressure. The corresponding dissociation degree of O_2, i.e. the number density of O divided by the maximum possible number density of O is shown in Fig. 21, indicating similar behavior.

The temperature attained by the gas is due to how much of the delivered energy goes into electronic and vibrational excitations, i.e. fast gas heating[54]. Although this calculation is considered beyond the scope of the present study, back of the envelope estimates can be readily made. The streamer phase is responsible for adding charge to the gas; only the remaining energy can be used to heat it up. This furnishes an upper limit given by [21]:

$$\Delta T \leq \frac{\epsilon_0 U_0^2}{r_m^2 log(l/r_m)\rho c_v} \tag{40}$$

where U_0 is the potential at the head of the streamer (which is very close to the breakdown voltage V_s, ρ is the density of the gas, and c_v is the specific heat capacity at constant volume. Say $U_0 \approx 6kV$, $r_m \approx 0.5\ mm$, $l \approx 1\ mm$, $\rho \approx 1\ kg/m^3$, and $c_v \approx 716J/kg/K$. This gives $\Delta T \leq 0.6\ K$, which is extremely small and justifies modeling streamer propagation as isothermal. If U_0 is increased to $10kV$, $\Delta T \leq 1.83\ K$, still a small value. It stands to reason that most of the heating takes place due to fast gas heating *after* the streamer has bridged the gap. A fraction of the delivered energy density is used for this; the exact fraction can be computed using methods discussed in

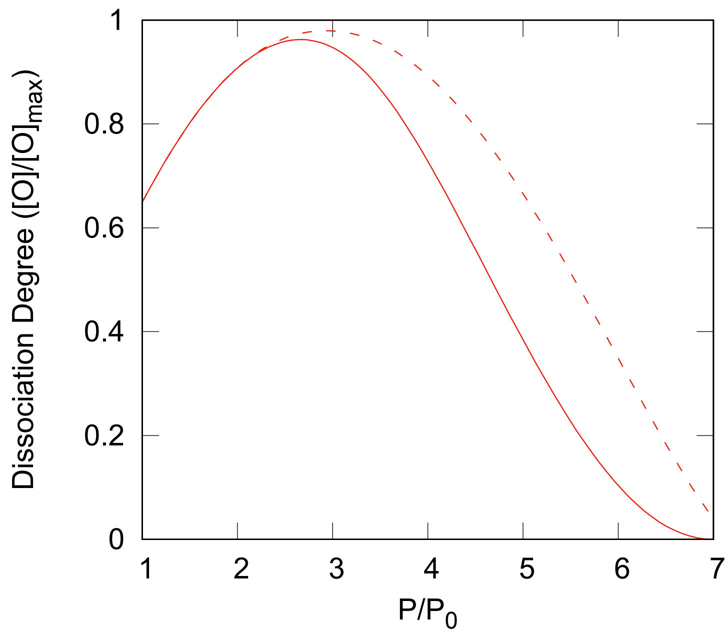

Figure 21. The dissociation degreeof O_2 as a function of pressure in the presence of a transmission line. The dashed lines correspond to the case where E_m/N is fixed as E_m/N_0.

[55]. From Fig. 20, the approximately $30mJ/m^3$ deposited to the gas at 1 atm translates to a maximum temperature increase of $\approx 35,000K$. However, this is an upper limit: not all the energy goes into heating of the channel: cathode fall losses, and radical formation (which can however recombine later to return some heat) take away much of the energy. Even if close to 10% makes it to the gas, temperatures in excess of 1000 K are certainly attainable when the applied voltage exceeds the breakdown voltage. However, for SI engines, it is not sufficient to simply reach a high temperature and locally ignite the mixture: in order for a flame to sustain its propagation outwards, the streamer radius must be greater than or equal to the critical radius of the flame. This problem becomes particularly acute for lean and dilute fuel-air mixtures. The reader is referred to a recent study conducted on the problem of sustained flame propagation in the context of low temperature plasma discharges for more information [56].

5. Summary

A simple circuit model was developed for the purpose of understanding energy delivery from a pulsed voltage source to a non-equilibrium plasma discharge. The model comprises a small set of parameters that determine streamer breakdown, its propagation, electron and radical production, and the cathode fall. The streamer head radius and field are the most difficult to measure and thus serve as model parameters suitable for sensitivity studies. It is found that energy delivery is very sensitive to the parameters governing the aforementioned phenomena, often giving rise to non-monotonic behavior. The transmission line was found to play a significant role in the energy loading of the gas, yielding energy delivery characteristics significantly different from cases where it is absent. Lastly, cylinder compression was found to yield an optimal energy loading, indicating that a discharge system designed for one pressure will not work optimally at others.

The present model is intended to be used with in-cylinder combustion simulations, with sufficient room for tuning to match coarse grained experiments. Future work aims at addressing the effects of multiple pulses by taking into account the thermodynamic evolution of the gas from pulse to pulse. Model refinements are anticipated to be largely driven by discoveries made in the detailed numerical simulation of such discharges.

6. Acknowledgements

Argonne National Laboratory's work was supported by the U.S. Department of Energy, Office of Energy Efficiency and Renewable Energy, Office of Vehicle Technology under contract DE-AC02-06CH11357. The authors wish to thank the DOE Technology Managers Michael Weismiller and Kevin Stork, and the DOE Program Manager Gurpreet Singh, for funding this research. We are also grateful to the reviewers who helped improve the quality of the manuscript in various parts.

7. Appendix

The following list summarizes the values for the various coefficients encountered in the present work:

(i) **Eq. 7:** $a_0 = 823.983$, $a_1 = 15965.3$, $a_2 = -1.65014$, $a_3 = 0.05734$, $a_4 = -7.803 \times 10^{-4}$, $a_5 = 3.78846 \times 10^{-6}$.

(ii) **Eq. 13:** $a_0 = 3 \times 10^{10}$, $a_1 = -1.92944 \times 10^{17}$, $a_2 = 2.40785 \times 10^{14}$, $a_3 = -1.22774 \times 10^{10}$, $a_4 = 3.66446 \times 10^{5}$, $a_5 = -6.078126$.

(iii) **Eq. 14:** $a_0 = 9.905226 \times 10^{-2}$, $a_1 = -2.780622 \times 10^{2}$, $a_2 = 0.866119$, $a_3 = -7.913062 \times 10^{-5}$, $a_4 = 3.3533161 \times 10^{-9}$, $a_5 = -5.5127 \times 10^{-14}$.

(iv) **Eq. 16:** $a_0 = 1.13914 \times 10^{-17}$, $a_1 = -4.215968 \times 10^{-19}$, $a_2 = -3.175575 \times 10^{-22}$, $a_3 = 2.437596 \times 10^{-24}$, $a_4 = -7.074965 \times 10^{-28}$, $a_5 = 6.538064 \times 10^{-32}$.

(v) **Eq. 21:** For O radical production, $a_0 = 6.551 \times 10^{-24}$, $a_1 = 8.440$, $a_2 = 4.667$, $a_3 = -0.252$. For $N_2(B)$ production, $a_0 = 5.485 \times 10^{-24}$, $a_1 = -225.432$, $a_2 = 2.973$, $a_3 = -0.201$.

(vi) **Eq. 24:** For O radicals, $a_0 = -8.136 \times 10^{15}$, $a_1 = 3.064 \times 10^{15}$, $a_2 = 1.798 \times 10^{13}$, $a_3 = -5.138 \times 10^{9}$, $a_4 = 6.709 \times 10^{5}$, $a_5 = -34.2$. For $N_2(B)$, $a_0 = -1.194 \times 10^{17}$, $a_1 = 2.964 \times 10^{16}$, $a_2 = 6.462 \times 10^{12}$, $a_3 = -5.470 \times 10^{6}$, $a_5 = -69.152$.

(vii) **Eq. 31:** $a_0 = 1.929285 \times 10^{24}$ and $a_1 = 0.99892$.

References

[1] Fei Wang, JB Liu, J Sinibaldi, C Brophy, A Kuthi, C Jiang, P Ronney, and Martin A Gundersen. Transient plasma ignition of quiescent and flowing air/fuel mixtures. *IEEE Transactions on Plasma Science*, 33(2):844–849, 2005.

[2] James Sevik, Thomas Wallner, Michael Pamminger, Riccardo Scarcelli, Dan Singleton, and Jason Sanders. Extending lean and exhaust gas recirculation-dilute operating limits of a modern gasoline direct-injection engine using a low-energy transient plasma ignition system. *Journal of Engineering for Gas Turbines and Power*, 138(11):112807, 2016.

[3] Douglas Breden, Anand Karpatne, and Laxminarayan Raja. Modelling of electrode erosion for prediction of spark plug lifetime. Technical report, SAE Technical Paper, 2018.

[4] James P Szybist, Stephen Busch, Robert L McCormick, Josh A Pihl, Derek A Splitter, Matthew A Ratcliff, Christopher P Kolodziej, John ME Storey, Melanie Moses-DeBusk, David Vuilleumier, et al. What fuel properties enable higher thermal efficiency in spark-ignited engines? *Progress in Energy and Combustion Science*, 82:100876, 2021.

[5] Ather A Quader. What limits lean operation in spark ignition engines—flame initiation or propagation? *SAE Transactions*, pages 2374–2387, 1976.

[6] Riccardo Scarcelli, Thomas Wallner, Sibendu Som, Sayan Biswas, Isaac Ekoto, Douglas Breden, Anand Karpatne, and Laxminarayan L Raja. Modeling non-equilibrium discharge and validating transient plasma characteristics at above-atmospheric pressure. *Plasma Sources Science and Technology*, 27(12):124006, 2018.

[7] Vyaas Gururajan, Riccardo Scarcelli, Anand Karpatne, Douglas Breden, Laxminarayan Raja, Sayan Biswas, and Isaac Ekoto. A computational study of the thermodynamic conditions leading to autoignition in nanosecond pulsed discharges. In *Internal Combustion Engine Division Fall Technical Conference*, volume 59346, page V001T06A009. American Society of Mechanical Engineers, 2019.

[8] Jaehong Kim and Richard W Anderson. Spark anemometry of bulk gas velocity at the plug gap of a firing engine. *SAE transactions*, pages 2256–2266, 1995.

[9] CG Suits and H Poritsky. Application of heat transfer data to arc characteristics. *Physical Review*, 55(12):1184, 1939.

[10] JM Duclos and O Colin. Arc and kernel tracking ignition model for 3d spark-ignition engine calculations. In *The Proceedings of the International symposium on diagnostics and modeling of combustion in internal combustion engines 01.204*, page 46. The Japan Society of Mechanical Engineers, 2001.

[11] T. Huiskamp, S. Subramanian, V. Gururajan, W. P. Schroeder, C. A. Schroeder, M. A. Gundersen, and S. B. Cronin. Boosting the energy efficiency of a nanosecond pulsed corona plasma system with a multiple-wire plasma reactor. *IEEE Transactions on Plasma Science*, 48(1):245–257, jan 2020.

[12] Sa I Braginskii. Theory of the development of a spark channel. *Sov. Phys. JETP*, 34:1068–1074, 1958.

[13] Jannis Teunissen, Anbang Sun, and Ute Ebert. A time scale for electrical screening in pulsed gas discharges. *Journal of Physics D: Applied Physics*, 47(36):365203, 2014.

[14] Jannis Teunissen. Improvements for drift-diffusion plasma fluid models with explicit time integration. *Plasma Sources Science and Technology*, 29(1):015010, 2020.

[15] GK Grubert, MM Becker, and D Loffhagen. Why the local-mean-energy approximation should be used in hydrodynamic plasma descriptions instead of the local-field approximation. *Physical Review E*, 80(3):036405, 2009.

[16] J. Teunissen. *3D simulations and analysis of pulsed discharges*. PhD thesis, Department of Applied Physics, 11 2015. Proefschrift.

[17] Maria Castela, Benoît Fiorina, Axel Coussement, Olivier Gicquel, Nasser Darabiha, and Christophe O Laux. Modelling the impact of non-equilibrium discharges on reactive mixtures for

simulations of plasma-assisted ignition in turbulent flows. *Combustion and flame*, 166:133–147, 2016.

[18] Vyaas Gururajan, Riccardo Scarcelli, Sayan Biswas, and Isaac Ekoto. Cfd modeling of low temperature ignition processes from a nanosecond pulsed discharge at quiescent conditions. In *Internal Combustion Engine Division Fall Technical Conference*. American Society of Mechanical Engineers, 2021.

[19] Igor V Adamovich, Munetake Nishihara, Inchul Choi, Mruthunjaya Uddi, and Walter R Lempert. Energy coupling to the plasma in repetitive nanosecond pulse discharges. *Physics of Plasmas*, 16(11):113505, 2009.

[20] Yu P Raizer. *Gas Discharge Physics*. Springer Berlin, 1983.

[21] Eduard Meerovič Bazelyan and Yu P Raizer. *Spark discharge*. Routledge, 2017.

[22] Leonard Benedict Loeb and John M Meek. *The mechanism of the electric spark*. Stanford University Press, 1941.

[23] GJM Hagelaar and LC Pitchford. Solving the boltzmann equation to obtain electron transport coefficients and rate coefficients for fluid models. *Plasma Sources Science and Technology*, 14(4):722, 2005.

[24] GJM Hagelaar. Brief documentation of bolsig+ version 03/2016. *Laboratoire Plasma et Conversion dEnergie (LAPLACE), Universit Paul Sabatier*, 118, 2016.

[25] S Pancheshnyi, S Biagi, MC Bordage, GJM Hagelaar, WL Morgan, AV Phelps, and LC Pitchford. The lxcat project: Electron scattering cross sections and swarm parameters for low temperature plasma modeling. *Chemical Physics*, 398:148–153, 2012.

[26] Lxcat phelps database. `www.lxcat.net/Phelps`. Accessed: 2021-04-15.

[27] Cornelius Lanczos. *Applied analysis*. Courier Corporation, 1988.

[28] Jorge J Moré. The levenberg-marquardt algorithm: implementation and theory. In *Numerical analysis*, pages 105–116. Springer, 1978.

[29] Thomas Williams, Colin Kelley, and many others. Gnuplot 4.6: an interactive plotting program. `http://gnuplot.sourceforge.net/`, April 2013.

[30] Vizglow. `https://esgeetech.com/products/vizglow-plasma-modeling/`. Accessed: 2021-04-15.

[31] Afivo-streamer. `https://teunissen.net/afivo_streamer/`. Accessed: 2021-04-15.

[32] Tat Loon Chng, IS Orel, SM Starikovskaia, and IV Adamovich. Electric field induced second harmonic (e-fish) generation for characterization of fast ionization wave discharges at moderate and low pressures. *Plasma Sources Science and Technology*, 28(4):045004, 2019.

[33] Alejandro Luque, Valeria Ratushnaya, and Ute Ebert. Positive and negative streamers in ambient air: modelling evolution and velocities. *Journal of Physics D: Applied Physics*, 41(23):234005, 2008.

[34] IA Kossyi, A Yu Kostinsky, AA Matveyev, and VP Silakov. Kinetic scheme of the non-equilibrium discharge in nitrogen-oxygen mixtures. *Plasma Sources Science and Technology*, 1(3):207, 1992.

[35] S Achat, Y Teisseyre, and E Marode. The scaling of the streamer-to-arc transition in a positive point-to-plane gap with pressure. *Journal of Physics D: Applied Physics*, 25(4):661, 1992.

[36] GV Naidis. Simulation of streamer-to-spark transition in short non-uniform air gaps. *Journal of physics D: Applied physics*, 32(20):2649, 1999.

[37] David Z Pai, Deanna A Lacoste, and Christophe O Laux. Transitions between corona, glow, and spark regimes of nanosecond repetitively pulsed discharges in air at atmospheric pressure. *Journal of Applied Physics*, 107(9):093303, 2010.

[38] Vyaas Gururajan and Fokion N Egolfopoulos. Transient plasma effects on the autoignition of dme/o2/ar and c3h8/o2/ar mixtures. *Proceedings of the Combustion Institute*, 36(3):4165–4174, 2017.

[39] Ratko K Janev, William D Langer, E Douglass Jr, et al. Elementary processes in hydrogen-helium plasmas: cross sections and reaction rate coefficients. 2012.

[40] DL Rusterholtz, DA Lacoste, GD Stancu, DZ Pai, and CO Laux. Ultrafast heating and oxygen

dissociation in atmospheric pressure air by nanosecond repetitively pulsed discharges. *Journal of Physics D: Applied Physics*, 46(46):464010, 2013.

[41] Thierry Poinsot and Denis Veynante. *Theoretical and numerical combustion*. RT Edwards, Inc., 2005.

[42] Richard P Brent. *Algorithms for minimization without derivatives*. Courier Corporation, 2013.

[43] William Shockley. Currents to conductors induced by a moving point charge. *Journal of applied physics*, 9(10):635–636, 1938.

[44] R Morrow and N Sato. The discharge current induced by the motion of charged particles in time-dependent electric fields; sato's equation extended. *Journal of Physics D: Applied Physics*, 32(5):L20, 1999.

[45] Stanford Goldman. *Transformation calculus and electrical transients*. Prentice-Hall, 1949.

[46] RB Spielman and Y Gryazin. Screamer: an optimized pulsed-power circuit-analysis tool. In *2016 IEEE International Power Modulator and High Voltage Conference (IPMHVC)*, pages 269–274. IEEE, 2016.

[47] FH Branin. Transient analysis of lossless transmission lines. *Proceedings of the IEEE*, 55(11):2012–2013, 1967.

[48] Peter Fritzson. *Principles of object-oriented modeling and simulation with Modelica 3.3: a cyber-physical approach*. John Wiley & Sons, 2014.

[49] Richard Pavelle, Michael Rothstein, and John Fitch. Computer algebra. *Scientific American*, 245(6):136–153, 1981.

[50] Alan C Hindmarsh, Peter N Brown, Keith E Grant, Steven L Lee, Radu Serban, Dan E Shumaker, and Carol S Woodward. Sundials: Suite of nonlinear and differential/algebraic equation solvers. *ACM Transactions on Mathematical Software (TOMS)*, 31(3):363–396, 2005.

[51] William H Press, Saul A Teukolsky, William T Vetterling, and Brian P Flannery. Numerical recipes in c, 1988.

[52] Peter Fritzson, Adrian Pop, Karim Abdelhak, Adeel Asghar, Bernhard Bachmann, Willi Braun, Daniel Bouskela, Robert Braun, Lena Buffoni, Francesco Casella, et al. The openmodelica integrated environment for modeling, simulation, and model-based development. *Modeling, Identification and Control*, 41(4):241–295, 2020.

[53] Michelangelo Balmelli, Raphael Färber, Laura Merotto, Patrik Soltic, Davide Bleiner, Christian M Franck, and Jürgen Biela. Experimental analysis of breakdown with nanosecond pulses for spark-ignition engines. *IEEE Access*, 9:100050–100062, 2021.

[54] NA Popov. Fast gas heating in a nitrogen–oxygen discharge plasma: I. kinetic mechanism. *Journal of Physics D: Applied Physics*, 44(28):285201, 2011.

[55] A Flitti and S Pancheshnyi. Gas heating in fast pulsed discharges in n2–o2 mixtures. *The European Physical Journal Applied Physics*, 45(02):21001, 2009.

[56] Vyaas Gururajan, Sayan Biswas, Riccardo Scarcelli, and Isaac Ekoto. Cfd modeling of low temperature ignition processes from a nanosecond pulsed discharge at quiescent conditions. In *ASME 2021 Internal Combustion Engine Division Fall Technical Conference*. American Society of Mechanical Engineers, 2021.